PAPER

Check for updates

Photon-avalanche for developing a high-sensitivity 3D-printed optical temperature sensor

Christian Hernández-Álvarez, [ID] *[ab] Inocencio R. Martín, [ID] *[a] Tomasz Grzyb[b] and Fernando Rivera-López [ID] [c]

Photon avalanche (PA) is a phenomenon that generates intense emission under optical excitation in a weak absorption region of materials, particularly those doped with lanthanide ions such as thulium ions (Tm^{3+}). Although PA behavior in various Tm^{3+}-doped matrices has been previously investigated, this study proposes a different approach, *i.e.*, using a different excitation wavelength (1060 nm) to observe and analyze the emission dynamics in order to focus its application as a highly sensitive temperature sensor in various media, such as air and isopropanol. LnF_3–ZnF_2–SrF_2–BaF_2–TmF_3 glass ceramic doped with Tm^{3+} was used to ensure the high effectiveness of the PA process and obtain intense emission. The choice of the glass ceramic also made it possible to prevent emission quenching in the proposed resin-based thermometer. Emission spectroscopy techniques were employed under varying excitation powers and temperatures to characterize the luminescence intensity ratio (LIR) and its correlation with temperature. The results demonstrate that the Tm^{3+}-doped system exhibits avalanche behavior with relative sensitivities ranging from 0.01 to 4.9% K^{-1} within the 299 to 354 K temperature range. Moreover, the uncertainty in temperature estimation remained low, between 0.67 and 0.32 K. These findings prove that Tm^{3+}-doped glasses are promising candidates for developing precise and reliable optical sensors across various applications.

1. Introduction

The upconversion (UC) phenomenon involves the absorption of two or more photons, typically in the infrared range, resulting in light emission at shorter wavelengths, such as visible or ultraviolet light.[1–3] This nonlinear optical process has garnered considerable attention due to its potential applications in biological imaging, photovoltaics, and laser technologies.[4–9] Among the mechanisms that enable UC, we can find excited-state absorption (ESA), energy transfer upconversion (ETU), photon-avalanche (PA), *etc.*[10,11] Specifically, PA involves the initial absorption of a low-energy photon, which triggers a series of energy transfers that significantly amplify luminescent emission.[3,12,13] In this mechanism, the initial photon absorption increases the population of electrons in an intermediate energy state, followed by energy transfers and positive feedback loops that result in intense light emission.[14,15] The PA process is particularly useful in applications requiring high detection sensitivity and signal amplification, such as optical sensors and laser devices.[16–18] However, the main drawback of the photon-avalanche process lies in the need for precise excitation conditions to trigger the phenomenon, which can limit its practical applicability in some instances.[14,15]

Lanthanide (Ln^{3+}) ions are commonly used as dopants in luminescent materials, also those showing an upconversion phenomenon.[19–21] They possess unique electronic properties due to the nature of f–f electronic transitions, like narrow absorption and emission lines, high values of luminescence lifetimes ranging to tens of milliseconds, large Stokes (or anti-Stokes) shifts, and the ladder-like energy levels structure, which make them ideal for various optical applications.[22–26] Another property of Ln^{3+} ions is their temperature-dependent luminescence. The ratio between Ln^{3+} emission lines has been widely utilized in remote temperature sensors.[25] There are many examples of bioapplications of Ln^{3+}-based temperature sensors as they offer emission and excitation lines within biological transparency windows.[27–29]

Among Ln^{3+} ions, thulium (Tm^{3+}), erbium (Er^{3+}), and holmium (Ho^{3+}) ions are particularly effective in inducing photon-avalanche

[a] Universidad de La Laguna, Departamento de Física, MALTA-Consolider Team, IMN. Apdo. Correos 456, E-38206, San Cristóbal de La Laguna, Santa Cruz de Tenerife, Spain. E-mail: chernaal@ull.edu.es, imartin@ull.edu.es

[b] Adam Mickiewicz University, Faculty of Chemistry, Uniwersytetu Poznańskiego 8, 61-614 Poznań, Poland. E-mail: chrher1@amu.edu.pl

[c] Universidad de La Laguna, Departamento de Ingeniería Industrial, Escuela Superior de Ingeniería y Tecnología. Apdo. Correos 456, E-38206, San Cristóbal de La Laguna, Santa Cruz de Tenerife, Spain

9332 | *J. Mater. Chem. C*, 2025, **13**, 9332–9338

This journal is © The Royal Society of Chemistry 2025

phenomena.[30–33] In particular, Tm^{3+} is known for its transitions between energy levels that result in emissions in the infrared range, making it ideal for temperature sensors and optical communication applications.[14,15,30,33]

PA holds promising applications across various technological fields.[34,35] In optical sensors, the high detection sensitivity offered by PA enables the development of exact temperature measurements. These sensors can detect minute temperature variations based on changes in the luminescence of Ln^{3+}-doped materials.[16–18,36] Furthermore, PA is used in signal amplification for optical communication systems, enhancing the efficiency and range of data transmissions.[36] PA can improve imaging techniques in the medical field, providing higher resolution and contrast in visualizing biological structures.[36–38] Current research is also exploring the use of PA in developing solid-state lasers and advanced optoelectronic devices, leveraging its capacity to generate intense and controlled emissions.[36,39]

Recently, interesting optical devices have been developed employing additive manufacturing (AM) technology.[40] In this sense, Zheng *et al.*[41] reported 3D-printed units that exhibit intense mechanoluminescence in response to mechanical impact and friction. Runowski *et al.*[42] fabricated 3D-printed polymers for high-resolution anti-counterfeiting and latent fingerprint detection.[43] Concerning sensors' applications, in previous work, we reported a luminescent gear manufactured by 3D printing that incorporates optically active nanoparticles in resin.[44] Following these novelty researches, a new remote optical temperature sensor is fabricated in this work, combining AM with a photo-curable polymer.

This study focuses on characterizing the photon-avalanche process in Tm^{3+}-doped glasses and evaluating their potential as high-sensitivity temperature sensors. We used the glass ceramic to ensure high emission intensity. In contrast to nanoparticles or nanopowders, glasses, and bulk crystals are less prone to quenching processes due to defects in the structure or surface-related interactions with the surrounding environment.[13] Through a series of experiments, we investigated the luminescent emission dynamics under varying excitation and temperature conditions. Additionally, we developed a model to correlate the luminescence intensity ratios with temperature, providing precise calibration of the material for practical applications. We propose a 3D-printed resin-based sensor containing luminescent particles to determine the temperature of the selected environment. We aim to demonstrate these materials' viability as reliable optical sensors and explore their applicability in diverse environments such as air and isopropanol.

2. Experimental section

2.1. Materials and synthesis

The initial composition for preparing the sample, given in mol%, was $(40-x)LnF_3$, $20ZnF_2$, $20SrF_2$, $20BaF_2$, $xTmF_3$, where x was set to 2.5. All chemicals used had a minimum purity of 99.5%. The mixture corresponding to this composition was first heated at 673 K for one hour with $NH_4F \cdot HF$ to ensure the conversion of any residual oxides into fluorides. Afterward, the mixture was melted at 1446 K. The molten material was then cast into an aluminum mold preheated to 796 K, producing glass plates with a thickness of 1–2 mm.[30]

A natural 3D850 SMARTFIL polylactic acid (PLA) filament of 1.75 mm in diameter from Smart Materials 3D was used to manufacture the temperature sensor. The prototype was designed with Tinkercad software, and the digital design was exported in surface tessellation language (STL) format. The STL file was imported to the Bambu Studio slicer to select the manufacturing parameters and generate the G-code file. Finally, the specimen was printed by fused deposition modeling (FDM) using a Bambu Lab X1 Carbon printer. During manufacturing, fixed parameters were layer width of 0.4 mm, layer height of 0.2 mm, 100% infill pattern density, bed temperature of 323 K, extruder temperature of 493 K, and deposition speed of 30 mm s^{-1} for the base and 25 mm s^{-1} for the sensor part.

The resin employed was a Simple Siraya Tech, which consists of a mixture composition of urethane acrylate (CAS no. 877072-28-1, wt% = 20–50%), acrylic monomer (CAS no. 64401-02-1, wt% = 30–60%), and photoinitiator (CAS no. 119-61-9, wt% = 0–5%). The resin was doped with the optically active material, which was initially ground using a mortar to reduce its size and then processed in a ball mill for 1 hour at 600 rpm in reversing mode to ensure homogeneous milling and obtain a powder. The doped resin was then coupled to the PLA specimen and cured under an UV lamp at 365 nm.

A small piece was fabricated and submerged in isopropanol for two weeks to control the stability in service of this temperature sensor. After this period, it was verified that the sample did not lose any mass and the geometric was perfectly preserved.
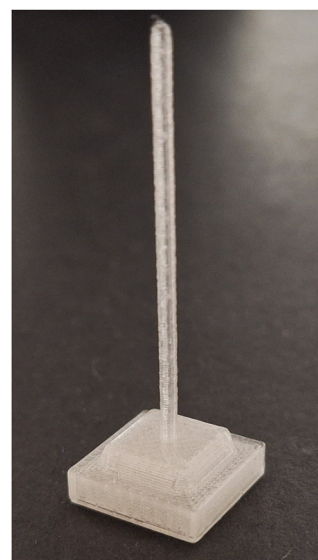

Fig. 1 Temperature sensor fabricated using fluorindate glass through 3D printing.

This journal is © The Royal Society of Chemistry 2025

J. Mater. Chem. C, 2025, **13**, 9332–9338 | **9333**

The experiment ensures the use of the prototype as a temperature sensor in this aqueous medium (see Fig. 1)

2.2. Characterization

A tunable CW Ti:sapphire laser system (Spectra Physics 3900S) pumped by a 532 nm laser (Spectra-Physics Millenia) and tuned to 1060 nm was used to excite the sample. The excitation intensity was varied by changing the laser power, and the Gaussian beam was focused on the sample with a 20 mm lens. The waist spot size on the sample (defined as the $1/e^2$ radius of the intensity) was shown to be 5.6×5.6 μm^2. The temporal evolution measurements were obtained by modulating the beam with a mechanical chopper and using a LeCroy oscilloscope. The laser power was monitored using an Ophir StarLite power meter. The emission spectra within the visible range were captured using an Andor Shamrock 500 spectrometer coupled with the silicon and InGaAs Andor Newton CCD cameras. The sample was heated using a Linkam system (THMS600). For the temperature measurements with the printed sensor, a thermostatically controlled water bath was used to heat the liquid-containing cuvette.

3. Results and discussion

3.1. Photon-avalanche process

In the photon-avalanche process, the material absorbs energy in a weak absorption region with an excitation wavelength of 1060 nm, and through energy transfer mechanisms between its energy levels, an intense emission is produced. Emission peaks were observed at 475 nm ($^1G_4 \rightarrow {}^3H_6$), 800 nm ($^3H_4 \rightarrow {}^3H_6$), 1460 nm ($^3H_4 \rightarrow {}^3F_4$), and 1625 nm ($^3F_4 \rightarrow {}^3H_6$), with our study focusing on the latter two emissions (see Fig. 2a and b). It should be noted that the $^3F_4$ level can be populated significantly through phonon decay and *via* 1460 nm radiative decay. Additionally, an electron in the ground state can be excited to this level by cross-relaxation, leading to a photon-avalanche process when conditions are right.

Fig. 3a illustrates how the emission band's rise time and luminescence intensity at 475 nm depend on the excitation power. It is observed that around 142 mW of excitation power, the response time shifts from increasing to decreasing. Additionally, the dependence of luminescence intensity on excitation power changes, with slopes of $s = 2.90$ and $s = 10.07$, indicating a shift in the number of photons required for the emission of 475 nm, placing the sample in the PA region.[14,15,18,36,39] These are clear indicators of avalanche processes, suggesting a power threshold for photon-avalanche initiation.[14,15,18,36,39] Fig. 3b shows the temporal evolution curves at three different excitation powers (83 mW, 142.5 mW, and 279 mW), illustrating the changes in emission behavior as the excitation power varies. The inset in Fig. 3b presents a three-dimensional graph of the luminescence intensity increase, showing how the material's response varies with excitation power and time. This behavior is critical for understanding the relaxation and energy transfer processes within the Tm^{3+}-doped material.[14,15,18,36,39]

3.2. Temperature sensor

Once the photon-avalanche regime is reached, the emission spectrum in the infrared range can be obtained. Fig. 4a shows the characteristic emission peaks of the Tm^{3+} ion in the IR region.[45,46] These peaks correspond to transitions between different energy levels $^3H_4 \rightarrow {}^3F_4$ (1460 nm) and $^3F_4 \rightarrow {}^3H_6$ (1625 nm). It is observed that, as the temperature increases, the emission at 1460 nm decreases. This is due to the higher probability of the $^3H_4$ level decaying non-radiatively to the $^3F_4$ level through phonon interactions.

Additionally, the population of the $^3F_4$ level increases because of the cross-relaxation process occurring during the avalanche process. This level then emits radiatively at 1625 nm (spectra normalized to the emission at 1625 nm). Parameters such as the luminescence intensity ratio (LIR) were used to characterize an optical sensor based on luminescence, representing the luminescence intensity ratio (1625 nm/1460 nm). As photon-avalanche processes are complex and involve multiple
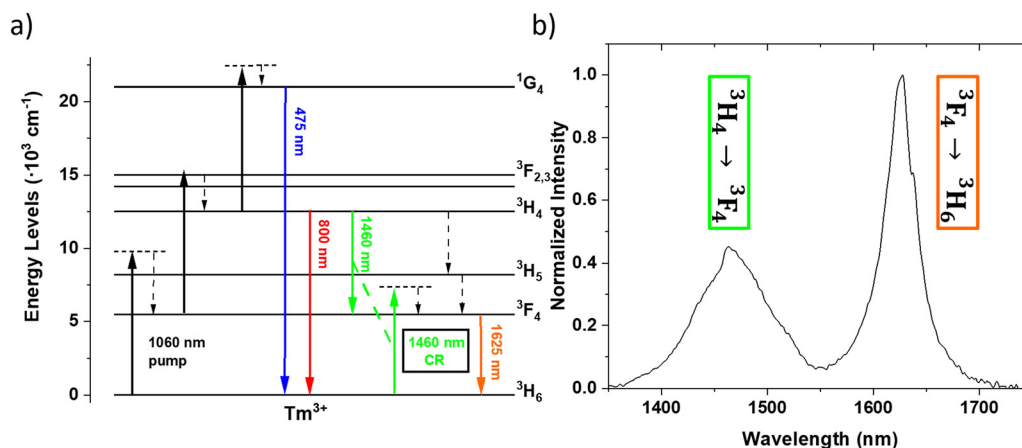

Fig. 2 (a) Energy level diagram of Tm^{3+} illustrating the photon-avalanche process under 1060 nm excitation. (b) Near-infrared emission spectrum of studied material under 1060 nm excitation.
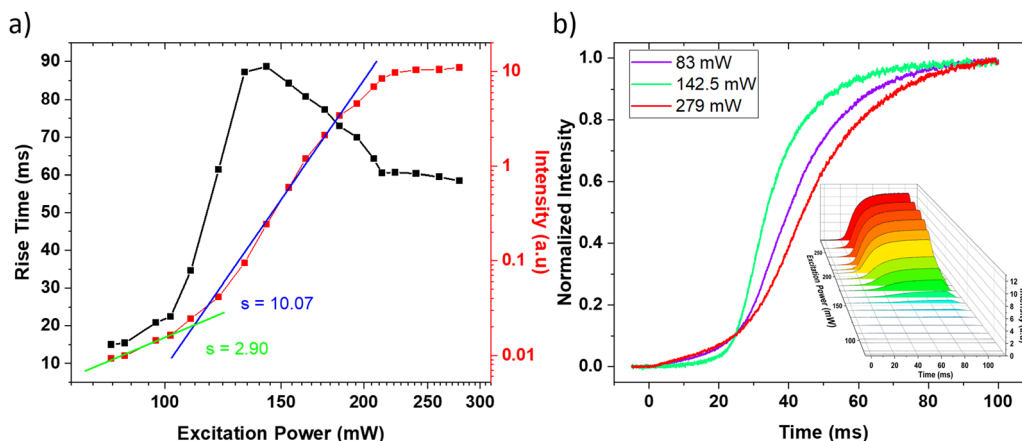
9334 | *J. Mater. Chem. C*, 2025, **13**, 9332–9338

This journal is © The Royal Society of Chemistry 2025

Fig. 3 (a) Rise time and fluorescence intensity as a function of excitation power. (b) Temporal evolution curves for three different excitation powers. Inset: Three-dimensional graph of fluorescence intensity increase from excitation at $t = 0$ ms.
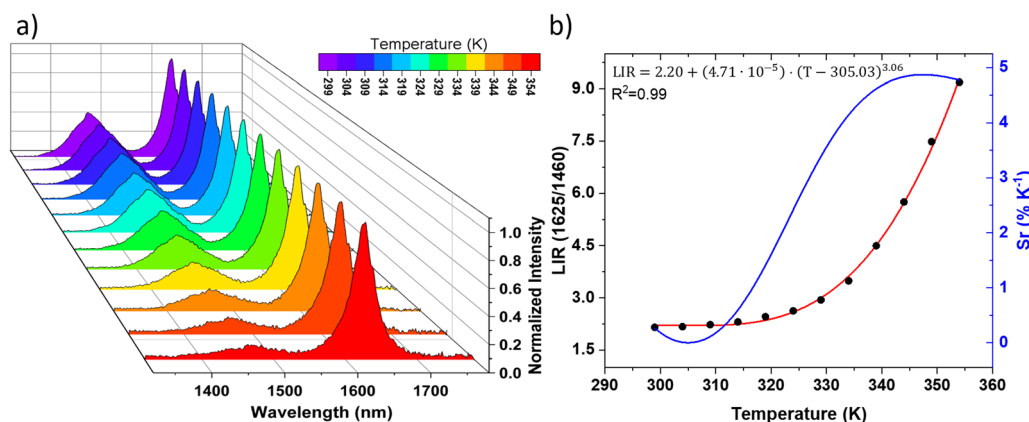

Fig. 4 (a) Emission spectrum in the IR range under 1060 nm excitation. (b) LIR and relative sensitivity as a function of temperature.

Table 1 Comparison of performance of different luminescent thermometers using the photon-avalanche

Host	Ln^{3+}	Temperature range [K]	Maximum S_r [% K^{-1}]	λ [nm]	Ref.
Fluoroindate glass	Tm	299–354	4.9	1625/1460	This work
YAG	Nd	273–573	5.3	800	16
$LiLaP_4O_{12}$	Nd	300–573	5.6	800	16
Y_2O_3	Nd	300–573	7.1	800	16
GdO_3	Nd	300–573	6.7	800	16
$GdYO_3$	Nd	300–573	7.0	800	16
$NaYF_4{:}Ln^{3+}$ @$NaYF_4$	Yb, Pr	98–273	7	607	17
			7.5	482	
		98–448	4.3	607	
			4.3	482	
$NdVO_4$	Yb, Er	298–618	3.5	750/853	18

parameters, the fitting equation $f(T)$ was proposed empirically to correlate the LIR with temperature, thereby calibrating the material for future experiments.

$$\text{LIR} \equiv \frac{I_{1625}}{I_{1460}} = f(T) \qquad (1)$$

In order to compare the sensitivity of the sample with other commonly used luminescent temperature sensors, the relative sensitivity (S_r) given by the following formula was calculated:

$$S_r(T) = 100\% \times \frac{1}{\text{LIR}} \frac{d\text{LIR}}{dT} \qquad (2)$$

The values obtained change from 0.01 to 4.9% K^{-1} in the range of temperatures studied, *i.e.*, from 299 to 354 K (Fig. 4b), cannot be compared with other results because no literature is

This journal is © The Royal Society of Chemistry 2025

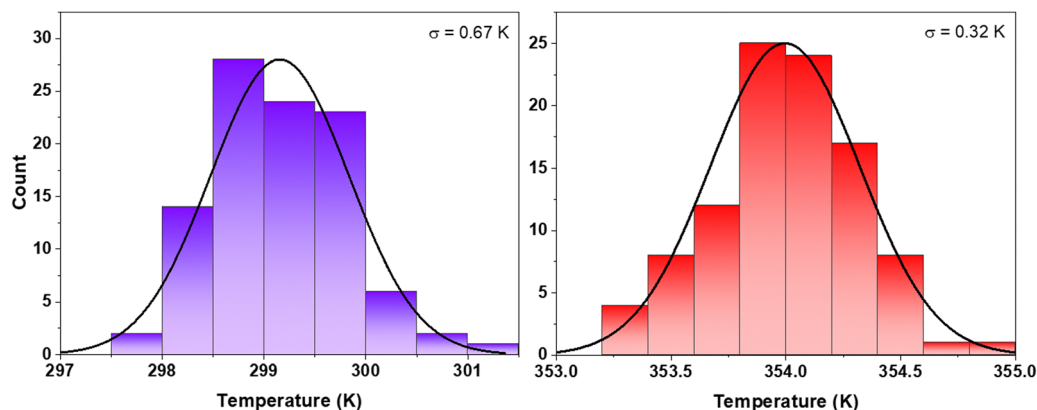*J. Mater. Chem. C*, 2025, **13**, 9332–9338 | **9335**

Fig. 5 Histograms of the measurement error for the lowest and highest temperatures.

available on temperature sensors using the photon-avalanche process in Tm^{3+}. To the best of our knowledge, this is the first reported temperature sensor based on the photon-avalanche process in Tm^{3+}. On the other hand, Table 1 presents a compilation of different materials and their respective dopants, providing a general reference for the temperature ranges and
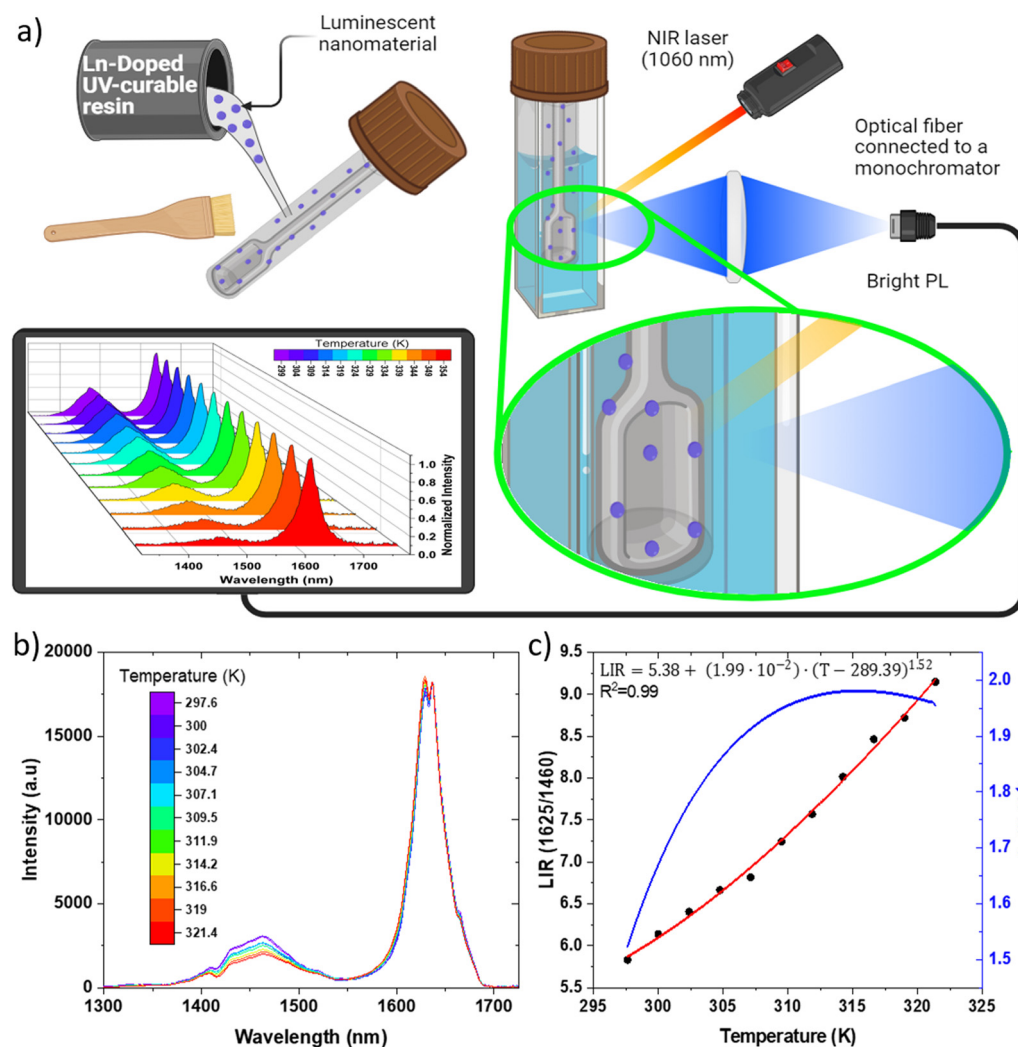

Fig. 6 (a) Diagram presenting the application of the photon-avalanche effect in liquid temperature measurement. (b) Infrared emission spectrum for the sample immersed in isopropanol (excited at 800 nm). (c) Corresponding LIR and relative sensitivity.

9336 | J. Mater. Chem. C, 2025, 13, 9332–9338

This journal is © The Royal Society of Chemistry 2025

relative sensitivities associated with temperature sensors utilizing the photon-avalanche phenomenon.

The use of a sensor also depends on the uncertainty in estimating the temperature change. An experimental estimation of this error was performed by recording 100 spectra under the same conditions at different temperatures (299 K and 354 K), repeating the measurements 100 times at each temperature point (see Fig. 5). The resulting standard deviation ranged between 0.67 and 0.32 K.

3.3. Liquid temperature control

Achieving the photon-avalanche condition requires precise control of the working system, which can present specific challenges. These requirements might limit its direct implementation in practical applications, particularly in maintaining the necessary excitation power to induce the phenomenon. However, it can be achieved for suitable applications and systems without significant difficulty, depending on the environment and intended use. In the diagram shown in Fig. 6a, we propose using 3D printing to create a resin support embedded with luminescent particles. By exciting these particles (to induce photon-avalanche), the infrared emission spectrum of the sample immersed in isopropanol is obtained (see Fig. 6b). This approach provides insights into how the environment affects calibration, as the surrounding liquid may absorb the emission bands. In Fig. 6c, the variation of the LIR and S_r as a function of the solvent (isopropanol) temperature is shown, highlighting changes in LIR behavior (ranging from 5.86 to 9.17) and S_r (varying between 1.52 and 1.98% K^{-1}) when the medium is altered. These values differ from those observed in Fig. 4b. This underscores the potential applications of this material as a temperature sensor in different media using the photon-avalanche effect, provided that a new calibration is performed for each specific medium.

4. Conclusions

In summary, we have characterized the photon-avalanche process in a fluorindate glass doped with Tm^{3+} and evaluated its potential as a temperature sensor receiving high sensitivity. The experiments demonstrated that the photon-avalanche phenomenon in these materials can be utilized to detect temperature variations with high precision, achieving a relative sensitivity of up to 4.9% K^{-1}, with a temperature measurement uncertainty ranging between 0.67 and 0.32 K. The practical application of the obtained sensor for temperature measurement in air and isopropanol was also explored, demonstrating the versatility of these materials in different environments. These results open new possibilities for using lanthanide-doped materials in optical sensor technologies and other advanced optoelectronic devices by applying the photon-avalanche effect.

Data availability

Data are available upon request from the authors.

Conflicts of interest

There are no conflicts of interest to declare.

Acknowledgements

References

1 J. Zhou, Q. Liu, W. Feng, Y. Sun and F. Li, 2015, preprint, American Chemical Society, DOI: **10.1021/cr400478f**.

2 D. Kang, E. Jeon, S. Kim and J. Lee, *Biochip J.*, 2020, **14**, 124–135.

3 F. Auzel, *Chem. Rev.*, 2004, **104**, 139–174.

4 Y. Liu, D. Tu, H. Zhu and X. Chen, *Chem. Soc. Rev.*, 2013, **42**, 6924–6958.

5 C. Hernández-Álvarez, G. Brito-Santos, I. R. Martín, J. Sanchiz, K. Saidi, K. Soler-Carracedo, Ł. Marciniak and M. Runowski, *J. Mater. Chem. C*, 2023, **11**, 1221–1229.

6 C. Chen, C. Li and Z. Shi, *Adv. Sci.*, 2016, **3**, 1600029.

7 G. Brito-Santos, B. Gil-Hernández, I. R. Martín, R. Guerrero-Lemus and J. Sanchiz, *RSC Adv.*, 2020, **10**, 27815–27823.

8 G. Brito-Santos, C. Hernández-Rodríguez, B. Gil-Hernández, B. González-Díaz, I. R. Martín, R. Guerrero-Lemus and J. Sanchiz, *Dalton Trans.*, 2022, **51**, 3146–3158.

9 X. Chen, D. Peng, Q. Ju and F. Wang, *Chem. Soc. Rev.*, 2015, **44**, 1318–1330.

10 K. N. Shinde, S. J. Dhoble, H. C. Swart and K. Park, 2012, pp. 41–59.

11 M. Safdar, A. Ghazy, M. Lastusaari and M. Karppinen, *J. Mater. Chem. C Mater.*, 2020, **8**, 6946–6965.

12 A. Skripka, M. Lee, X. Qi, J.-A. Pan, H. Yang, C. Lee, P. J. Schuck, B. E. Cohen, D. Jaque and E. M. Chan, *Nano Lett.*, 2023, **23**, 7100–7106.

13 M. Dudek, M. Szalkowski, M. Misiak, M. Ćwierzona, A. Skripka, Z. Korczak, D. Piątkowski, P. Woźniak, R. Lisiecki, P. Goldner, S. Maćkowski, E. M. Chan, P. J. Schuck and A. Bednarkiewicz, *Adv. Opt. Mater.*, 2022, **10**, 2201052.

14 C. Lee, *Photon avalanching in Tm³⁺:NaYF₄ nanocrystals and its applications*, PhD thesis, Columbia University, 2022.

15 M. Majak, M. Misiak and A. Bednarkiewicz, *Mater. Horiz.*, 2024, **11**, 4791–4801.

This journal is © The Royal Society of Chemistry 2025

J. Mater. Chem. C, 2025, **13**, 9332–9338 | **9337**

16 L. Marciniak, A. Bednarkiewicz and K. Elzbieciak, *J. Mater. Chem. C Mater.*, 2018, **6**, 7568–7575.

17 Z. Korczak, M. Dudek, M. Majak, M. Misiak, Ł. Marciniak, M. Szalkowski and A. Bednarkiewicz, *Low Temp. Phys.*, 2023, **49**, 322.

18 Y. Li, S. Guan, R. Wang and Y. Li, *Ceram. Int.*, 2023, **49**, 35001–35010.

19 Z. Luo, D. Mao, X. Li, J. Luo, C. Gong and X. Liu, *Coord. Chem. Rev.*, 2024, **508**, 215773.

20 P. Yasaka and J. Kaewkhao, 2015 4th International Conference on Instrumentation, Communications, Information Technology, and Biomedical Engineering (ICICI-BME), 2015, pp. 4–15.

21 S. Wang and L. Wang, *TrAC, Trends Anal. Chem.*, 2014, **62**, 123–134.

22 M. A. Antoniak, S. J. Zelewski, R. Oliva, A. Żak, R. Kudrawiec and M. Nyk, *ACS Appl. Nano Mater.*, 2020, **3**, 4209–4217.

23 S. Goderski, M. Runowski, P. Woźny, V. Lavín and S. Lis, *ACS Appl. Mater. Interfaces*, 2020, **12**, 40475–40485.

24 T. Tröster, *Handbook on the Physics and Chemistry of Rare Earths*, 2003, 33, pp. 515–589.

25 C. D. S. Brites, A. Millán and L. D. Carlos, *Handbook on the Physics and Chemistry of Rare Earths*, 2016, 49, pp. 339–427.

26 M. Runowski, A. Shyichuk, A. Tymiński, T. Grzyb, V. Lavín and S. Lis, *ACS Appl. Mater. Interfaces*, 2018, **10**, 17269–17279.

27 N. Jurga, M. Runowski and T. Grzyb, *J. Mater. Chem. C Mater.*, 2024, **12**, 12218–12248.

28 M. Suta, Ž. Antić, V. Đorđević, S. Kuzman, M. D. Dramićanin and A. Meijerink, *Nanomaterials*, 2020, **10**, 543.

29 M. Quintanilla, M. Henriksen-Lacey, C. Renero-Lecuna and L. M. Liz-Marzán, *Chem. Soc. Rev.*, 2022, **51**, 4223–4242.

30 I. R. Martín, V. D. Rodríguez, Y. Guyot, S. Guy, G. Boulon and M.-F. Joubert, *J. Phys.: Condens. Matter*, 2000, **12**, 1507.

31 F. Lahoz, I. R. Martín and J. M. Calvilla-Quintero, *Appl. Phys. Lett.*, 2005, **86**, 051106.

32 F. Auzel and Y. Chen, *J. Lumin.*, 1995, **65**, 45–56.

33 M. Zhang, P. Huang, W. Zheng, X. Song, X. Shang, W. Zhang, D. Yang, X. Yi and X. Chen, *Nano Lett.*, 2023, **23**, 8576–8584.

34 Y. Liang, Z. Zhu, S. Qiao, X. Guo, R. Pu, H. Tang, H. Liu, H. Dong, T. Peng, L.-D. Sun, J. Widengren and Q. Zhan, *Nat. Nanotechnol.*, 2022, **17**, 524–530.

35 E. S. Levy, C. A. Tajon, T. S. Bischof, J. Iafrati, A. Fernandez-Bravo, D. J. Garfield, M. Chamanzar, M. M. Maharbiz, V. S. Sohal, P. J. Schuck, B. E. Cohen and E. M. Chan, *ACS Nano*, 2016, **10**, 8423–8433.

36 J. Huang, G. Wei, H. Wei and B. Zhou, *ACS Appl. Opt. Mater.*, 2024, **2**, 1841–1853.

37 M. Szalkowski, A. Bednarkiewicz, D. Piątkowski and S. Maćkowski, 2024 24th International Conference on Transparent Optical Networks (ICTON), 2024, 1–4.

38 A. Bednarkiewicz, E. M. Chan, A. Kotulska, L. Marciniak and K. Prorok, *Nanoscale Horiz.*, 2019, **4**, 881–889.

39 M.-F. Joubert, S. Guy, B. Jacquier and C. Linarés, *Opt. Mater.*, 1994, **4**, 43–49.

40 F. Rivera-López, M. M. L. Pavón, E. C. Correa and M. H. Molina, *Polymers*, 2024, **16**(13), 1867.

41 T. Zheng, M. Runowski, I. R. Martín, K. Soler-Carracedo, L. Peng, M. Skwierczyńska, M. Sójka, J. Barzowska, S. Mahlik, H. Hemmerich, F. Rivera-López, P. Kulpiński, V. Lavín, D. Alonso and D. Peng, *Adv. Mater.*, 2023, **35**, 2304140.

42 M. Runowski, P. Woźny, I. R. Martín, K. Soler-Carracedo, T. Zheng, H. Hemmerich, F. Rivera-López, J. Moszczyński, P. Kulpiński and S. Feldmann, *Adv. Funct. Mater.*, 2024, **34**, 2307791.

43 A. Drozdowski, D. Poelman, M. Runowski, H. Hemmerich, F. Rivera-López and T. Grzyb, *J. Mater. Chem. C Mater.*, 2024, **12**, 13040–13049.

44 C. Hernández-Álvarez, P. I. Martín-Hernández, I. R. Martín, F. Rivera-López, H. Hemmerich, M. Grzegorczyk, S. Mahlik and M. Runowski, *Adv. Opt. Mater.*, 2024, 2303328.

45 T. Grzyb, I. R. Martín and R. Popescu, *Nanoscale*, 2024, **16**, 1692–1702.

46 X. Yuan, E. Cui, K. Liu, Y. Jiang, X. Yang, J. Tang, L. Yang, X. Liao, Y. Zhao, W. Sun, Y. Liu and J. Liu, *Ceram. Int.*, 2022, **48**, 35141–35149.

9338 | *J. Mater. Chem. C*, 2025, **13**, 9332–9338

This journal is © The Royal Society of Chemistry 2025